



Modelling voltammetric data from electrochemical capacitors

Hannah M. Fellows^a, Marveh Forghani^a, Olivier Crosnier^b, Scott W. Donne^{a,*}

^a Discipline of Chemistry, University of Newcastle, Callaghan, NSW, 2308, Australia

^b Polytech'Nantes, Site de la Chantrerie, rue Christian Pauc BP 50609, 44306, Nantes Cedex 3, France



HIGHLIGHTS

- A model has been developed to analyze CV data from electrochemical capacitors.
- Model is based on the response of a series RC circuit to a linear potential sweep.
- Other components include redox process, electrode instability and resistance.
- Model validity is demonstrated on the aqueous manganese dioxide electrode.

ARTICLE INFO

Keywords:

Cyclic voltammetry
Electrochemical capacitors
Double layer capacitors
Pseudo-capacitance

ABSTRACT

Linear and cyclic voltammetry are common method for the characterization of electrochemical capacitor electrodes. Herewith we describe an approach to modelling voltammetric data to provide more detailed information about the electrode under study. The model is based upon the response of a series arrangement of a resistor and capacitor to a linearly changing potential to simulate a double layer capacitor. Also included is a term to account for redox processes in localized domains, electrode instability at the extremes of potential, as well as electrode resistance, each of which represent behaviour commonly encountered in electrochemical capacitors. Development of the model is presented, together with its application to the aqueous manganese dioxide electrode.

1. Introduction

1.1. Energy storage and electrochemical capacitors

The renewable and reliable production of energy is one of the great challenges faced by future society. The current energy supply picture has the combustion of fossil fuels still providing the bulk of energy supply across the world [1–3]. This is of course not sustainable into the future due to the limited reserves of fossil fuels available, as well as the negative impact fossil fuel combustion has on the environment [4,5]. As such, the development and implementation of more sustainable energy generation technologies is warranted.

In parallel with the need for the introduction of renewable energy technologies is the need for improved performance and efficient energy storage and conversion systems. These systems are required for many purposes including improving the quality of electrical output from renewable energy technologies, such as in large scale energy production from technologies such as solar and wind, as well as the direct replacement of fossil fuel powered systems, such as the internal combustion engine.

Energy can be stored in many different ways, and indeed fossil fuels are a means of chemical energy storage, albeit irreversible. One of the more attractive approaches is electrochemical energy storage and conversion in devices such as batteries, electrochemical capacitors and fuel cells [6]. Systems like these are relatively efficient, reliable, cost effective, rechargeable, and can provide satisfactory energy and power on demand. Of these approaches, energy storage and conversion in electrochemical capacitors is making considerable commercial headway [7,8]. These devices are typified by excellent power densities and cyclability; however, can be considered limited by a relatively poor specific energy density and cost per kWh stored [9]. These negative features are actually opportunities for improvement and considerable global effort is ongoing to address and improve these features.

1.2. Materials for electrochemical capacitors

Activated carbon is the incumbent material of choice for use in commercial electrochemical capacitors because of its high specific surface area and tuneable porosity. It is most often used in non-aqueous electrolytes such as 1.0 M tetraethylammonium tetrafluoroborate in

* Corresponding author.

E-mail address: scott.donne@newcastle.edu.au (S.W. Donne).

acetonitrile or propylene carbonate [10]; however, it has also been used effectively in aqueous electrolytes such as 0.5–1.0 M H₂SO₄ [11,12] or 1.5–6.0 M KOH [13–16]. The specific capacitance from activated carbon in non-aqueous electrolytes is typically less than 120 F/g [17], and perhaps slightly larger in aqueous electrolytes [17], meaning that its energy density is quite low (< 10 Wh/kg). Nevertheless, activated carbon-based systems demonstrate excellent power densities (up to 10⁴ W/kg) and cyclability (> 10⁵ cycles without any appreciable fade) [18–21]. Despite this popularity, activated carbon is certainly not the only allotrope of carbon to be explored in electrochemical capacitors. Other phases such as carbon nano-tubes [22], nano-fibres [23], fullerenes [24], and nano-onions [25] have been explored with varying degrees of success; however, from a cost-benefit perspective, activated carbon is most often superior [9].

To address these deficiencies in specific energy density considerable effort has been focused on finding new materials that exhibit higher specific capacitances. In this regard, redox active metal oxides such as ruthenium dioxide and manganese dioxide, and conducting polymers such as polypyrrole and polythiophene, and variants thereof, have attracted considerable attention [26,27]. For these types of materials specific capacitance values up to 1340 F/g for ruthenium dioxide [28] and over 1000 F/g for manganese dioxide thin films in aqueous media [29] have been reported. The performance of conducting polymers has been reported to be up to 300 F/g [30]. Clearly these materials present a case for their use as electrochemical capacitor electrode materials, and as such their commercial development is ongoing.

1.3. Charge storage mechanisms

The differences in performance reported for these classes of materials prompts a need to differentiate the charge storage mechanisms these materials exhibit. In general, there are two different charge storage mechanisms that these materials can undergo [31]. Firstly, at any electrode-electrolyte interface an electrical double layer is formed where surface charge present on the electrode is balanced by counter charge in the electrolyte. This charge storage mechanism is dominant for materials such as activated carbon in a non-aqueous medium where the high surface area of the activated carbon enables a large electrode-electrolyte interface, and hence considerable charge storage. Additionally, for these types of materials the pore size distribution is critical [32]. While the presence of micro-porosity increases the electrode-electrolyte interface, it does not allow for facile ion transport meaning performance will be limited [21]. Conversely, macro-porosity might enable facile ion transport, but at the expense of interfacial area. Therefore, a balance of pore sizes is needed to maximize interfacial area and ion transport, and hence maximize performance for a particular application [33,34].

Beyond charge storage in the double layer, further charge storage can be associated with redox processes at the interface, otherwise known as pseudo-capacitance [31,35]. Certainly the nature of the redox processes that can occur depends entirely on the electrode-electrolyte system being used; e.g., activated carbon in aqueous media can undergo redox processes involving oxidation or reduction of the carbon surface [13], whereas metal oxides such as ruthenium dioxide or manganese dioxide, traditionally considered as a battery material, can undergo redox cycling associated with the transition metal [36,37]. An additional important consideration here is the reversibility of the redox processes [38]. Electrochemical capacitors are typified by excellent cyclability, and so any hint of irreversibility in these redox processes, such as a result of structural changes in the metal oxide, or reaction between the electrode and electrolyte materials, will degrade the overall performance of the system with cycle number [39–41].

1.4. Performance assessment

Many different physical, chemical and electrochemical methods have been developed and used to characterize electrochemical

capacitor systems. Electrochemically, techniques such as cyclic voltammetry and galvanostatic charge-discharge cycling have all been used to determine system performance [42,43]. Mechanistic information from these techniques can be limited because the appearance of the voltammetric or galvanostatic data can be similar despite the apparent differences in charge storage mechanisms. To address this, other electrochemical techniques such as electrochemical impedance spectroscopy [44,45] and step potential electrochemical spectroscopy [12,46–50] have been used, with outcomes being able to more readily differentiate the apparent charge storage mechanisms.

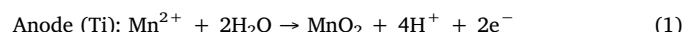
1.5. This work

In this work we report on the development of a modelling technique to extract more information from voltametric data collected on electrochemical capacitor materials. The focus of the work will be on a manganese dioxide electrode, although the method is generic for all other electrode types. It will enable the differentiation of charge storage mechanisms, particularly those involving redox processes in a uniform domain, as opposed to distributed redox reactions typical for pseudo-capacitance. It will also enable identification of electrode-electrolyte instabilities that could be detrimental to extended redox cycling.

2. Experimental

2.1. Electroactive materials

For the purposes of demonstrating the modelling procedure developed here an electrodeposited manganese dioxide (EMD) sample has been prepared for use as the cathode active working electrode in an electrochemical capacitor. This EMD was prepared by electrolysis of a hot (98 °C) acidic (0.3 M H₂SO₄) solution of manganese sulfate (1.0 M MnSO₄). The cell used for the electrolysis was based on an electrolyte-filled 2 L Pyrex beaker encased by a suitable heating mantle and temperature controller. Into this beaker were placed a flat titanium anode (exposed area 144 cm²), surrounded on both sides by two similarly sized copper cathodes to ensure a uniform current distribution. The cell electrolysis reactions were as follows:



The electrolysis was carried out at an anodic current density of 65 A/m² for sufficient time to make ~100 g of EMD. To counteract the consumption of Mn²⁺ and generation of H⁺, and so to maintain a constant electrolyte composition, a feed electrolyte of 1.5 M MnSO₄ was pumped into the electrolysis cell at an appropriate rate.

Once sufficient EMD had been electrodeposited onto the anodic substrate, the current was switched off and the electrodes removed immediately from the cell. When cool, the EMD was removed easily from the substrate by twisting the electrode to produce 1–2 cm diameter chunks of EMD. These chunks were suspended in 200 mL Milli-Q water, with the liquid phase adjusted to pH 7 by the addition of 0.1 M NaOH. This neutralization process was carried out as a first step towards removing any entrained electrolyte in the EMD. Once the pH had stabilized the EMD chunks were removed from the water and dried at 60 °C. The chunks were then milled in batches (30 s milling time to avoid excessive heat generation) using a Fritsch zirconia mill so as to pass through a 107 µm sieve. The powdered EMD was then re-suspended in 200 mL of Milli-Q water, with the pH of the suspension again adjusted so as to be stable at pH 7. Following this the suspension was filtered and washed thoroughly with Milli-Q water until the pH of the filtrate was the same as that of the wash water. The powdered EMD was then dried at 60 °C before storage in an airtight container.

The counter electrode material to be used in this study was an in-house prepared activated carbon. The first stage in the synthesis involved the pyrolysis of the biomass coconut shells at 800 °C under a flowing (100 mL/min) N₂ atmosphere in a tube furnace for 2 h. When cool, the intermediate biochar was then soaked in concentrated phosphoric acid (H₃PO₄) overnight and then activated by again heating at 800 °C under a flowing (100 mL/min) N₂ atmosphere in a tube furnace.

2.2. Electrode assembly and electrochemical protocol

The first step in electrochemical characterization was the preparation of an ink for casting. A dry mixture of 10% active material (EMD), 85% conductive carbon (Vulcan) and 5% binder (polyvinylidene difluoride, PVdF) was prepared. This high ratio of active material to conductive carbon was to ensure that the resultant electrode behaviour was dependent on just the active material, rather than the electrode construction. This dry mixture was then suspended 1:20 w/w in N-methylpyrrolidone (NMP) and stirred thoroughly to dissolve the PVdF and thus produce the ink. 50 µL of this ink was then pipetted and spread across the end of a previously polished (1200 grit) and cleaned 13 mm diameter, 5 cm long, vertically mounted stainless steel rod. This was then left to dry overnight at ambient temperature to evaporate the NMP solvent and thus produce the EMD-based, cathode-active working electrode. The active mass loading was 0.25 mg/cm². A similar procedure was used to prepare the counter electrode, except in this case the dry mixture consisted of 45% of the in-house prepared activated carbon, 45% conductive carbon (Vulcan), and 10% PVdF as the binder. After suspension (1:20 w/w) in NMP to prepare the ink, 100 µL of the

ink was drop-cast onto another vertically mounted, clean and polished 13 mm diameter, 5 cm long stainless steel rod. Drying overnight at ambient temperature removed the NMP solvent to produce an activated carbon counter electrode. Note the ratio of activated carbon to conductor and the larger volume of ink used here to ensure the counter electrode did not limit the overall cell performance.

The EMD-based working electrode and the activated carbon-based counter electrode were then inserted into opposite ends of the 13 mm perfluoroalkoxy (PFA) Swagelok T-junction, separated by two layers of a paper separator. The electrodes were then compressed under 250 MPa using a hydraulic ram and secured/sealed in place while still under load. This electrode assembly was then placed on a flat surface with the perpendicular port of the cell pointing upwards from the surface. The cell was then filled with 0.5 M K₂SO₄ electrolyte, and a saturated calomel reference electrode (SCE) sealed into place through the perpendicular port, ensuring no air bubbles were trapped in the cell. This assembled cell was then allowed to equilibrate for ~2 h.

The electrochemical protocol involved cycling the cell using cyclic voltammetry for 10 cycles at each scan rate, ranging from 100 to 10 mV/s.

3. Results and discussion

3.1. Voltametric data and performance

Cyclic voltamograms for the EMD electrode recorded at different scan rates are shown in Fig. 1. As expected, an increasing scan rate led to an increasing current [46,51]. By integrating the measured cathodic

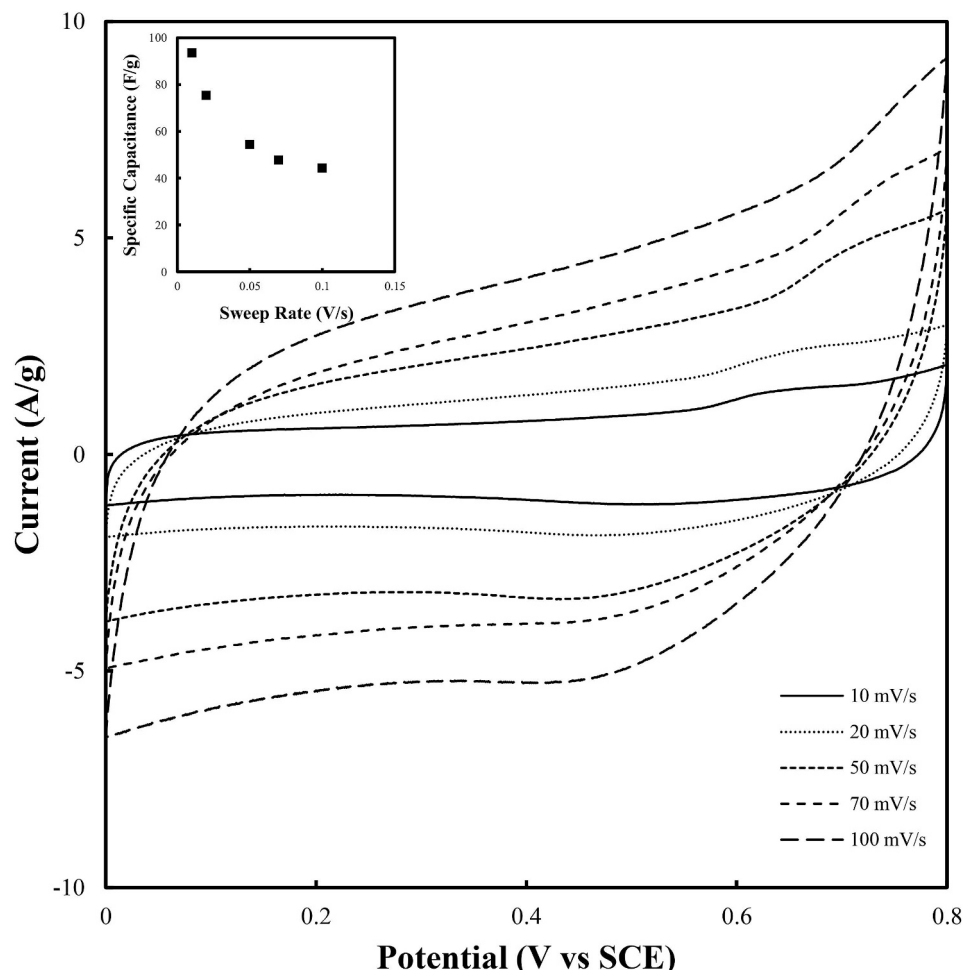


Fig. 1. Voltamograms of the manganese dioxide (EMD) electrode recorded at different scan rates. Inset: Cathodic specific capacitance as a function of scan rate.

current (i ; A/g) with respect to time (t ; s) for a particular scan rate (v ; V/s) the cathodic charge (q ; C/g) can be determined; i.e.,

$$q = \int_0^t idt = \frac{1}{v} \int_{E_1}^{E_2} idE \quad (4)$$

This can then be converted in to specific cathodic capacitance (C ; F/g) using:

$$C = \frac{q}{\Delta E} \quad (5)$$

where $\Delta E = E_2 - E_1$ is the potential window used (V). The inset in Fig. 1 shows the specific cathodic capacitance as a function of scan rate. So while the current may be increasing with an increasing scan rate, the overall electrode performance is declining. Although not shown in Fig. 1, the charge efficiency for each cycle was always very close to unity.

3.2. Model development

The voltametric data shown in Fig. 1, together with the associated determination of specific cathodic capacitance, essentially represents the extent to which data is commonly quantitatively analyzed in the literature. Qualitatively it may be stated that the data appears like the expected ‘box-like’ voltamogram typical of an electrochemical capacitor, although in this case the upward slope of the data towards higher potentials would indicate that the electrode is relatively resistive, and that there is evidence of a redox process at ~ 0.7 V in the anodic half-cycle. It is the intent of this work to develop a model that can be applied to voltametric data such as this to extract quantitative information related to these processes.

3.2.1. Double layer capacitance – series RC circuit

The first step towards modelling voltammetric data is to recognize that the observed behaviour can be represented by an electrical circuit, much in the same way as is done with electrochemical impedance spectroscopy (EIS) data. For the series arrangement of a resistor (R ; Ω .g) and capacitor (C ; F/g) the current response (i ; A/g) to an applied potential sweep (v ; V/s) is given by Ref. [52]:

$$i = vC \left[1 - \exp\left(-\frac{t}{RC}\right) \right] \quad (6)$$

Fig. 2(a)-(c) show the effect of a changing resistance, capacitance or scan rate on the resultant voltammetric data, respectively.

Increasing the series resistance (Fig. 2(a)) appears to have the effect of decreasing the rate at which the current responds to changes in potential, or in other words, the time constant (τ ; s) for the series RC arrangement, i.e.,

$$\tau = RC \quad (7)$$

A smaller resistance leads to a smaller time constant, and hence a faster response to the changing potential. For these plots it is also apparent that as the resistance increases there is less charge being passed, effectively diminishing the real capacitance (C_R ; F/g) of the electrode. To explore this further let us consider the fractional realizable capacitance (X_C) of the electrode relative to the ideal (C ; F/g); i.e.,

$$X_C = \frac{C_R}{C} \quad (8a)$$

Now, C_R can be determined from Eq. (6); i.e.,

$$C_R = \frac{q_{RC}}{\Delta E} = \frac{vC}{\Delta E} \int_0^t 1 - \exp\left(-\frac{t}{RC}\right) dt \\ = \frac{vC}{\Delta E} \left[t + RC \exp\left(-\frac{t}{RC}\right) - RC \right] \quad (8b)$$

where q_{RC} is the amount of charge passed for the series RC circuit (C/g), and ΔE is the potential window of the electrode (V). Therefore,

$$X_C = \frac{v}{\Delta E} \left[t + RC \exp\left(-\frac{t}{RC}\right) - RC \right] \\ = \frac{v}{\Delta E} \left[t + \tau \exp\left(-\frac{t}{\tau}\right) - \tau \right] \quad (9)$$

where the definition of the time constant (Eq. (7)) has been included into the expression. Now, typically when the capacitance is determined it is over the complete potential window used, which is a relatively long time compared to the time constant. Therefore, the exponential term in Eqn (9) will tend to zero. Additionally, if the value of time used is for the full potential window then $vt = \Delta E$; i.e.,

$$X_C (t \rightarrow \text{large}) = \frac{v}{\Delta E} (t - \tau) = 1 - \frac{v}{\Delta E} \tau \quad (10)$$

Thus, the fractional realizable capacitance is expected to decrease linearly with the time constant, as shown inset in Fig. 2(a). While this behaviour has been demonstrated here using changes in resistance, it is also valid for changes in capacitance as well.

Fig. 2(b) shows the effects of capacitance on the current response of the series RC circuit. As expected, an increase in capacitance gives rise to an increased plateau current. In general, the current plateau reached is equivalent to vC , which can be derived from Eq.(6), under the conditions of sufficiently long time. Increasing the capacitance also increases the time constant of the RC circuit, as per Eq.(7), meaning that the current response is relatively slower for the larger capacitance voltamograms. As mentioned above, Eq.(10) is also valid for changing capacitance values.

Fig. 2(c) shows the effect of scan rate on the voltammetric response of a series RC circuit. While the time constant for this system or electrode is the same in all these cases, what makes the voltammetric response different in each case is the degree of similarity between the time constant and the time-base of the experiment. For the data presented in this figure the time constant is 3.75 s. Compare this with the duration of the experiment at the different scan rates; i.e., 160, 80 and 16 s using scan rates of 0.005, 0.01 and 0.05 V/s. Here, when the time constant is similar to the duration of the experiment, the relative current response is slower.

3.2.2. Redox processes in a specific domain

Redox processes in the solid state or at the electrode-electrolyte interface that are associated with an energetically well-defined redox couple are not subject to semi-infinite mass transport conditions, such as commonly encountered for redox couples in solution. The reason for this is because the redox active species are present in a finite amount which is available in its entirety for charge transfer. An energetically well-defined redox couple is one in which a standard reduction potential can be defined for the redox reaction [53]. This is opposed to a delocalized system in which the redox processes, and hence charge, can be spread over a large potential window [54].

What is needed to model experimental data is an expression that represents the reduction or oxidation of a general redox couple [53] such as:



where Ox is the oxidized component and Red is the reduced component. The potential (E ; V) of this redox couple can be described by the Nernst equation [53]; i.e.,

$$E = E^\circ + \frac{RT}{nF} \ln \left(\frac{a(\text{Ox})}{a(\text{Red})} \right) \quad (12)$$

where E° (V) is the standard electrode potential for the redox couple that varies depending on the nature of the species undergoing the redox process, and $a(\text{Ox})$ and $a(\text{Red})$ are the activities of the oxidized and reduced species, respectively. All other terms have their usual electrochemical significance. Since there is a finite amount of Ox and Red present in the system and all is available for charge transfer, the

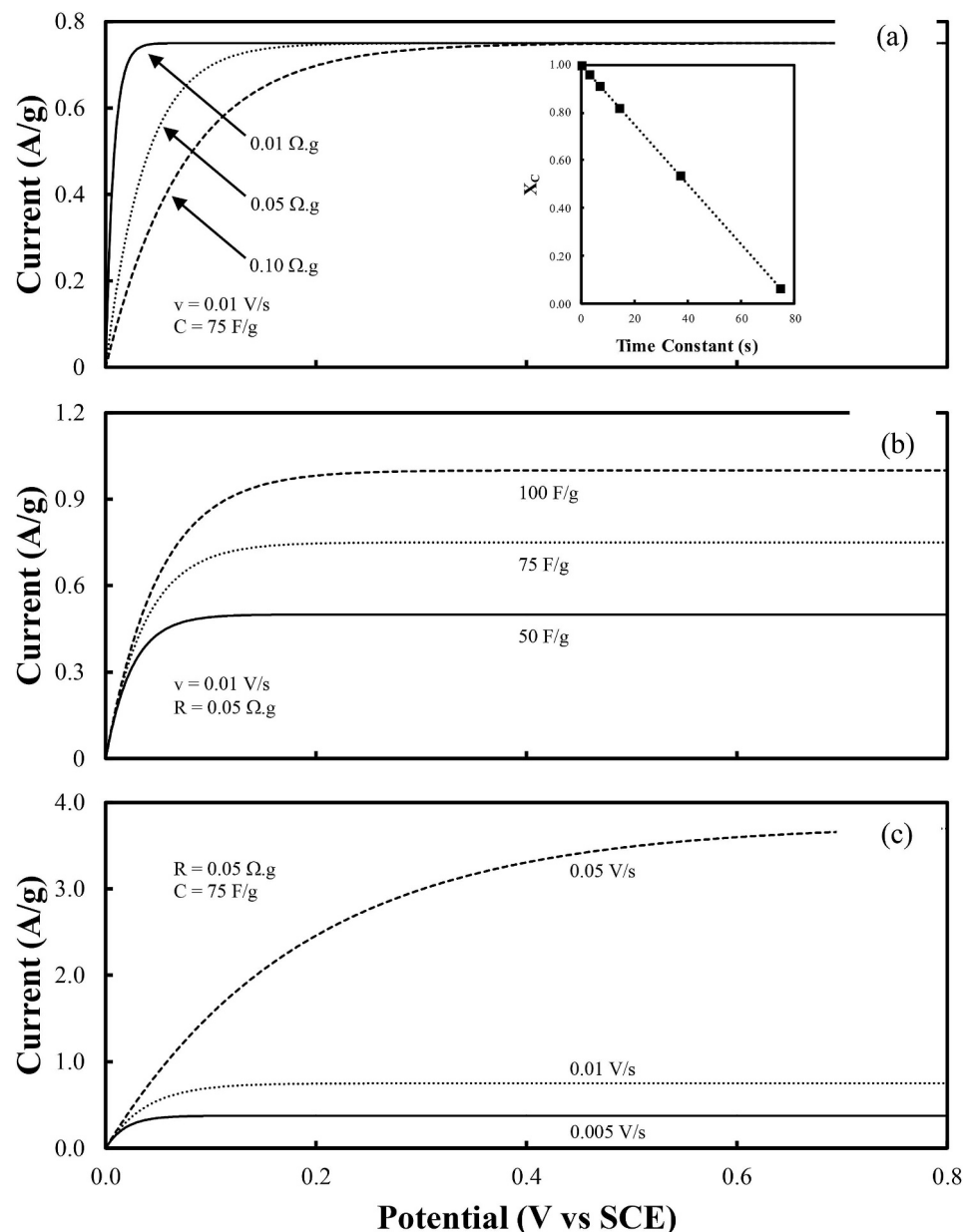


Fig. 2. Voltammetric behaviour of a series RC circuit as a function of (a) resistance (R ; $\Omega.g$), (b) capacitance (C ; F/g), and (c) scan rate (v ; V/s). Inset in (a): Plot of the fractional realizable capacitance as a function of time constant based on Eq.(10). These data were calculated using $v = 0.01 \text{ V/s}$ and $C = 75 \text{ F/g}$, with changing R values of 0.01, 0.05, 0.1, 0.2, 0.5 and $1.0 \Omega.g$.

activities of species can be replaced by mole fractions ($X(Ox)$) or X (Red); i.e.,

$$E = E^o + \frac{RT}{nF} \ln\left(\frac{X(Ox)}{X(\text{Red})}\right) \quad (13)$$

If we now assume that only the oxidized form of the redox couple is present initially, then with the passage of current, the amount of the reduced form produced is:

$$\text{moles of Red formed} = \frac{q}{nF} \quad (14)$$

where q is the amount of charge (C/g) passed. The moles of the oxidized form remaining is therefore:

$$\text{moles of Ox remaining} = M - \frac{q}{nF} \quad (15)$$

where M is the total number of moles of Ox and Red combined.

Substituting Eqns (14) and (15) into Eq.(13) gives:

$$E = E^o + \frac{RT}{nF} \ln\left(\frac{nMF - q}{q}\right) \quad (16)$$

which upon rearrangement gives:

$$q = \frac{nMF}{1 + \exp\left(\frac{nF}{RT}(E - E^o)\right)} \quad (17)$$

To adapt Eq.(17) for a linear sweep voltammetry experiment, we must realize that:

$$E = E_i + vt \quad (18)$$

where E_i is the initial potential for the voltammetry experiment (V), v is the scan rate (V/s), and t is the elapsed time (s). Making this substitution into Eq.(17) and also recognizing that:

$$i = \frac{dq}{dt} \quad (19)$$

then

$$i = \frac{d}{dt} \left[\frac{nMF}{1 + \exp(\frac{nF}{RT}(E_i + vt - E^o))} \right] = \frac{-\frac{n^2MF^2v}{RT} \exp(\frac{nF}{RT}(E_i + vt - E^o))}{\left[1 + \exp(\frac{nF}{RT}(E_i + vt - E^o)) \right]^2} \quad (20)$$

Note the minus sign in Eq.(20) represents a cathodic peak. Fig. 3 shows how the parameters in this expression (E^o , n, M and v) influence the appearance of the voltammetric peaks. Changing E^o changes the position of the peak, while n in this case is more an indicator of the kinetics of the redox process [53]. A very narrow peak, one representing a redox process occurring over a very narrow potential window, is given when n is relatively large, while a broad peak, perhaps indicative of sluggish reaction kinetics, occurs when n is small. Both M and v have similar effects in that they are directly proportional to the current flowing.

3.2.3. Electrode-electrolyte instabilities

Reactions that occur between the electrode material and the electrolyte in an electrochemical capacitor typically occur at the extremes of the potential window and are often irreversible in nature. Examples include hydrogen evolution and oxygen evolution in an aqueous media at low or high potentials, respectively. These types of activation controlled electrochemical reactions; i.e., reactions that are controlled by the potential at which they occur, or more specifically the overpotential, together with the abundance of reactants, particularly if the electrolyte is involved, can be described by the Butler-Volmer equation for electrochemical kinetics [55]; i.e.,

$$i = i_o \left[\exp\left(\frac{\alpha_a \eta F}{RT}\right) - \exp\left(-\frac{\alpha_c \eta F}{RT}\right) \right] \quad (21)$$

where i_o is the exchange current density (A/g), α_a and α_c are the anodic and cathodic transfer coefficients, respectively, and η is the overpotential (V). For the purposes of using this expression the overpotential is defined as $\eta = V - E^o$, where V is the applied potential (V) and E^o is the equilibrium potential for the process (V) used as a fitting parameter. For the application of this expression to the study of electrochemical capacitors only one of the terms in Eq.(21) will likely be used because as mentioned above, instability between the electrode material and the electrolyte typically occurs at the extremes of potential.

3.2.4. Electrode resistance

If we compare the experimental voltammetric data in Fig. 1 with that predicted from the series RC circuit in Fig. 2, it is apparent that the experimental data has an overall slope to it, as opposed to the constant current seen in the model data. Much is said in the literature regarding the resistance of electrochemical capacitor electrodes [56–59], and in the discussion of the series RC circuit it became clear what the effects of changing the resistance were. However, this does not account for the general upward slope of the experimental data. Therefore, what we will include here in model development is an ohmic-type resistance to account for the resistance of the electrode as a whole during the voltammetric experiment, as opposed to the resistance in the series RC circuit which appears to be more closely linked with the microscopic storage of charge. This ohmic resistance takes the form of a straight line in the voltammogram; i.e.,

$$i_{ohm} = \frac{E}{R_{ohm}} + K \quad (22)$$

where i_{ohm} is the current (A/g) resulting from the ohmic resistance of the electrode (R_{ohm} ; Ω.g), E is the applied electrode potential (V), and K is a constant taking into account the fact that the effects of the ohmic

resistance are not on an absolute scale, such as we would encounter in an electronic circuit, but instead are relative to the potential scale used here with respect to a reference electrode. When this component was modelled on experimental data two limitations were applied; i.e., (i) the ohmic current defined by Eq.(22) was set to zero when the actual experimental current was zero; and (ii) the slope of i_{ohm} was set to be the same for both the anodic and cathodic portions of the voltammetric cycle. These restrictions were applied to ensure that realistic fitting parameters were obtained.

3.3. Analysis of voltammetric data

We are now in the position to attempt to model the experimental data using each of the model characteristics described above. As such, the experimental voltammetric data was modelled using all of the components mentioned above, with the fitting accomplished using linear least squares regression. Fig. 4, contains the modelling result for the 10 mV/s scan on the manganese dioxide electrode.

For the anodic portion of the voltammogram (Fig. 4(a)) each of the characteristics discussed above are required. Firstly, the data appears to have a distinctly upwards slope, indicative of an overall resistive electrode (Eq.(22)). Secondly, there is a small anodic peak at ~0.7 V that can be modelled using Eq.(20). Thirdly, there is a need to include both anodic and cathodic Butler-Volmer expressions to account for the increasing in magnitude current at the upper and lower end of the potential window (Eq.(21)). Lastly, the voltammogram is built around the response of a series RC circuit, and so of course this has to be included (Eq.(6)). In this case the correlation coefficient (R^2) for the fitting was 0.9989. This value is typical of the closeness of fit achieved for all voltammetric data. During the cathodic portion of the voltammetric sweep (Fig. 4(b)) again all fitting components were used, although their appearance does not correspond to the reverse of the anodic sweep. The breakdown of the voltammetric data at different sweep rates is shown in Fig. 5(a)–(e) for the anodic half-cycle and Fig. 6(a)–(e) for the cathodic half-cycle, while the individual values for each component are listed in Tables 1–5. The calculated capacitance for each component in both the anodic and cathodic half-cycles has been determined using Eqns (4) and (5) and is shown in Tables 1–5, while their percent contribution to the overall capacitance is shown in Fig. 7(a) and (b).

3.3.1. Series RC circuit

The contributions made by the series RC circuit component to the total anodic and cathodic current is shown in Figs. 5(a) and 6(a), respectively.

During the anodic half cycle the current increases relatively rapidly to reach a plateau that increases with increasing sweep rate. This was to be expected based on Eq.(6). This behaviour was similar during the cathodic half-cycle; however, the increase in cathodic current was not as fast, with the current for only the two slowest sweep rates reaching a plateau value. The reason for the slower response was the higher series resistance for the cathodic half-cycle compared to the anodic half-cycle. This is also reflected in the time constant for the RC circuit component, which was on average 4.1 s for the anodic sweep compared to 8.4 s for the cathodic sweep. While the current flow for the series RC circuit was found to increase with sweep rate, the resultant capacitance was found to decrease due to inherent kinetic limitations associated with this charge storage process. This is reflected in the anodic and cathodic capacitance values in Table 1.

Charge storage in the manganese dioxide electrode is known to be due to a combination of both electrical double layer formation and pseudo-capacitance, both of which are associated with ion sorption at the electrode-electrolyte interface. Formation of the electrical double layer likely involves adsorption and desorption of cations on the oxide surface in response to electrical charge being added or removed from the interface, whereas the process of pseudo-capacitance involves redox processes involving the Mn^{4+}/Mn^{3+} couple together with delocalized

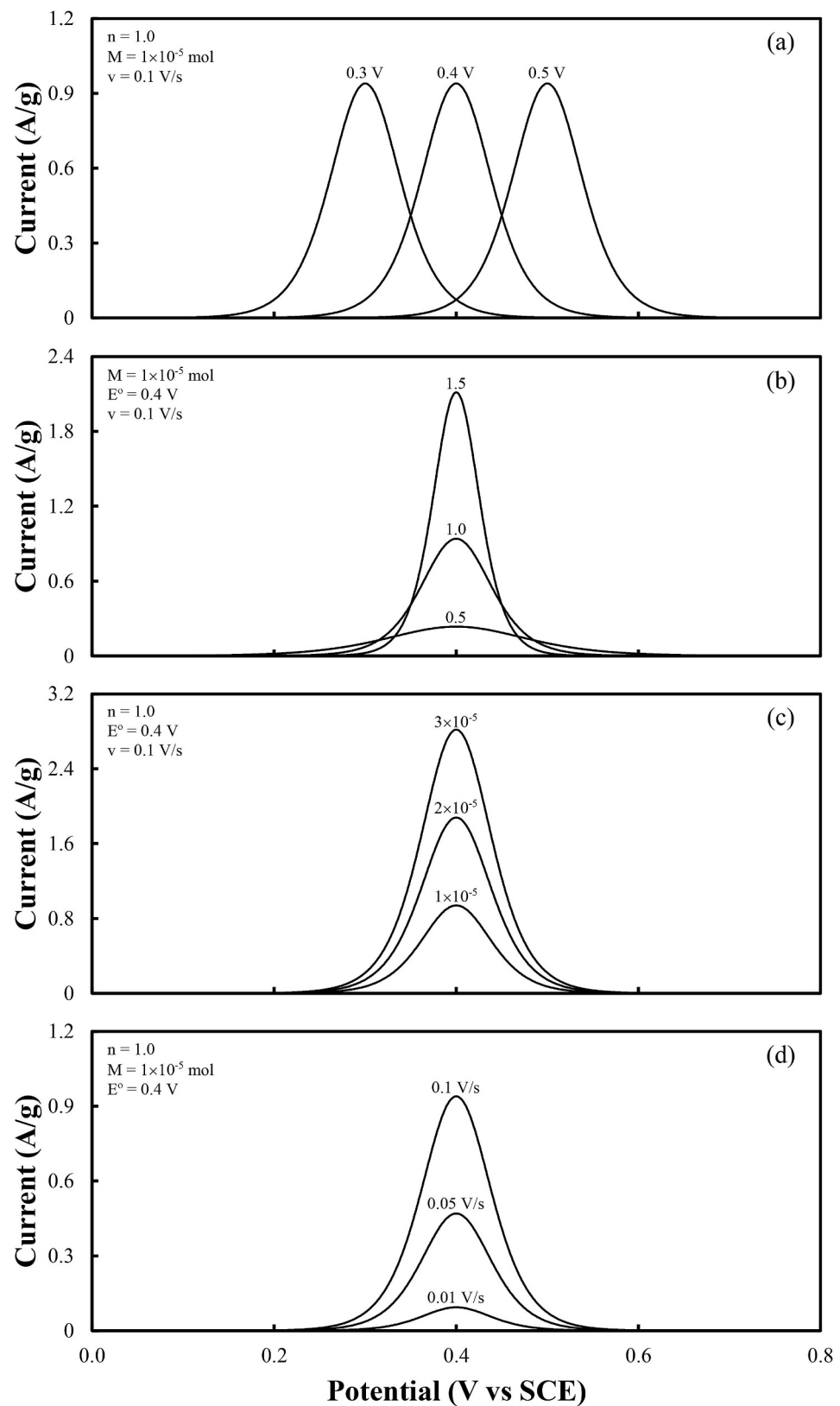


Fig. 3. Plot of Eq.(20) showing the effects of (a) E° , (b) n , (c) M , and (d) v on the appearance of the voltammetric peak.

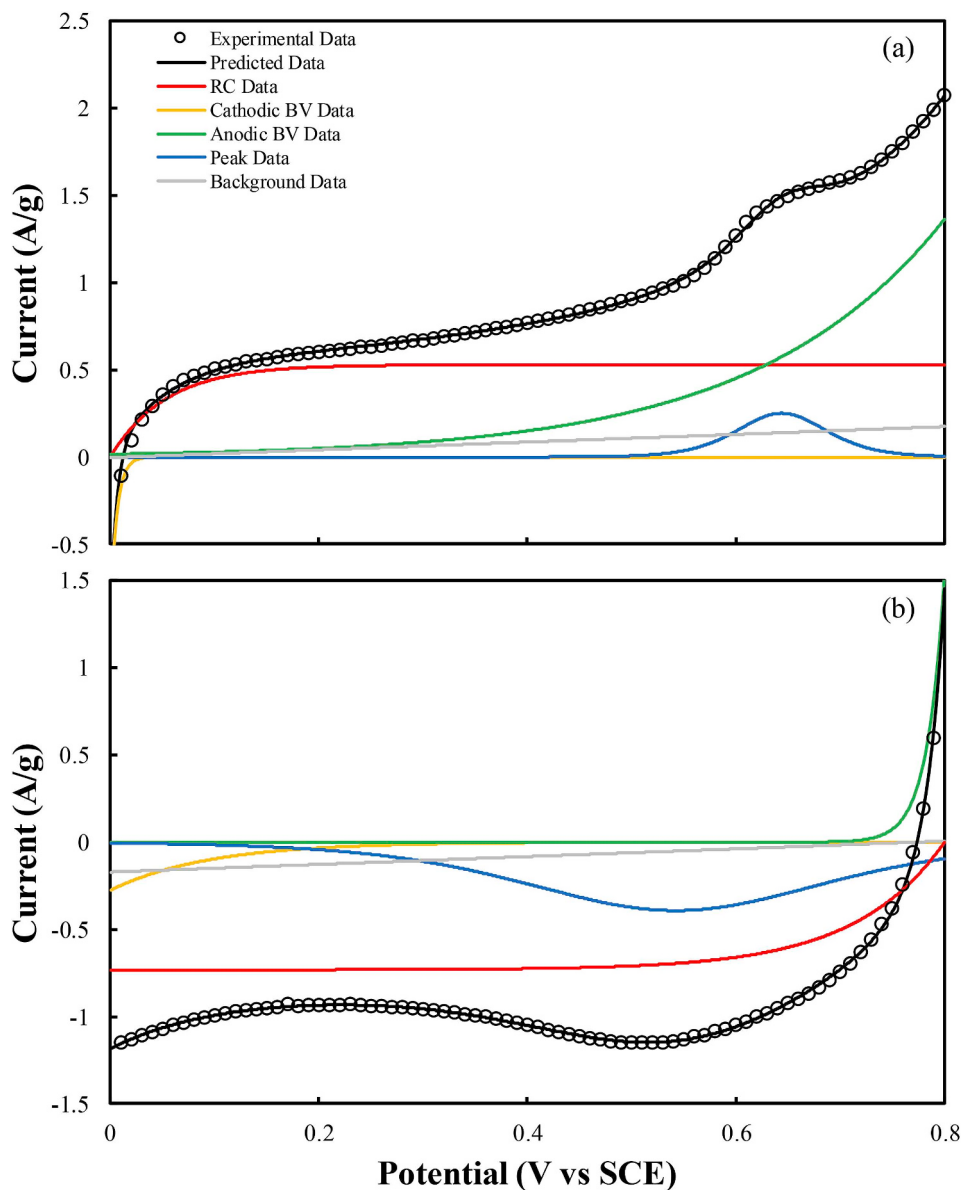
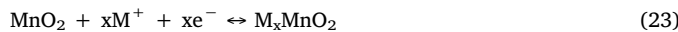


Fig. 4. Breakdown of the 10 mV/s scan on the manganese dioxide electrode into its individual components for (a) the anodic and (b) the cathodic half cycles. Here, BV refers to the use of the Butler-Volmer equation.

cation intercalation through the electrode-electrolyte interface; i.e.,



where M^+ represents the intercalated cation (K^+ or H^+ in this instance), and x indicates the fraction of charge associated with this process. The modelling results extracted here for the series RC circuit component would indicate that the oxidation process is more facile compared to the reduction process; i.e., it is kinetically easier to extract charge (M^+ and e^-) from the manganese dioxide electrode rather than intercalate it into the structure. With the large K^+ cation being used here it is not surprising that this is the case for the $\gamma\text{-MnO}_2$ (EMD) phase.

Also shown in Table 1 is a comparison between the modelled capacitance (C ; F/g) and the real capacitance (C_R ; F/g) determined through the use of Eqns (4) and (5). In all cases the real capacitance was less than the modelled capacitance. This is due to the series resistance present in the process diminishing the ability of the system to realize its full capacitance; i.e., X_C (Eq.(8)). It was found that the ability of the

processes occurring to achieve the full capacitance was diminished at higher sweep rates, again indicating the kinetic limitations of the processes. This was considerably worse for the cathodic processes, again due to the higher associated resistance. The fractional realizable capacitance (X_C) is also shown in Table 1, calculated using both direct means (Eq.(8)) and by approximation (Eq.(10)). For the anodic sweep the values of X_C from both methods were comparable because the series resistance was relatively low and the resultant current achieved its plateau value. However, for the cathodic sweep there was considerable divergence due to the increased resistance and the corresponding increase in time constant.

Fig. 7 shows that the series RC component is the greatest contributor to the overall capacitance, contributing on average $\sim 57\%$ during the anodic half-cycle and $\sim 59\%$ during the cathodic half-cycle. Systematically, its contributions are the greatest at both high and low sweep rates, likely due to the presence of other charge storage processes at more localized potentials rather than across the full potential window as the RC component does.

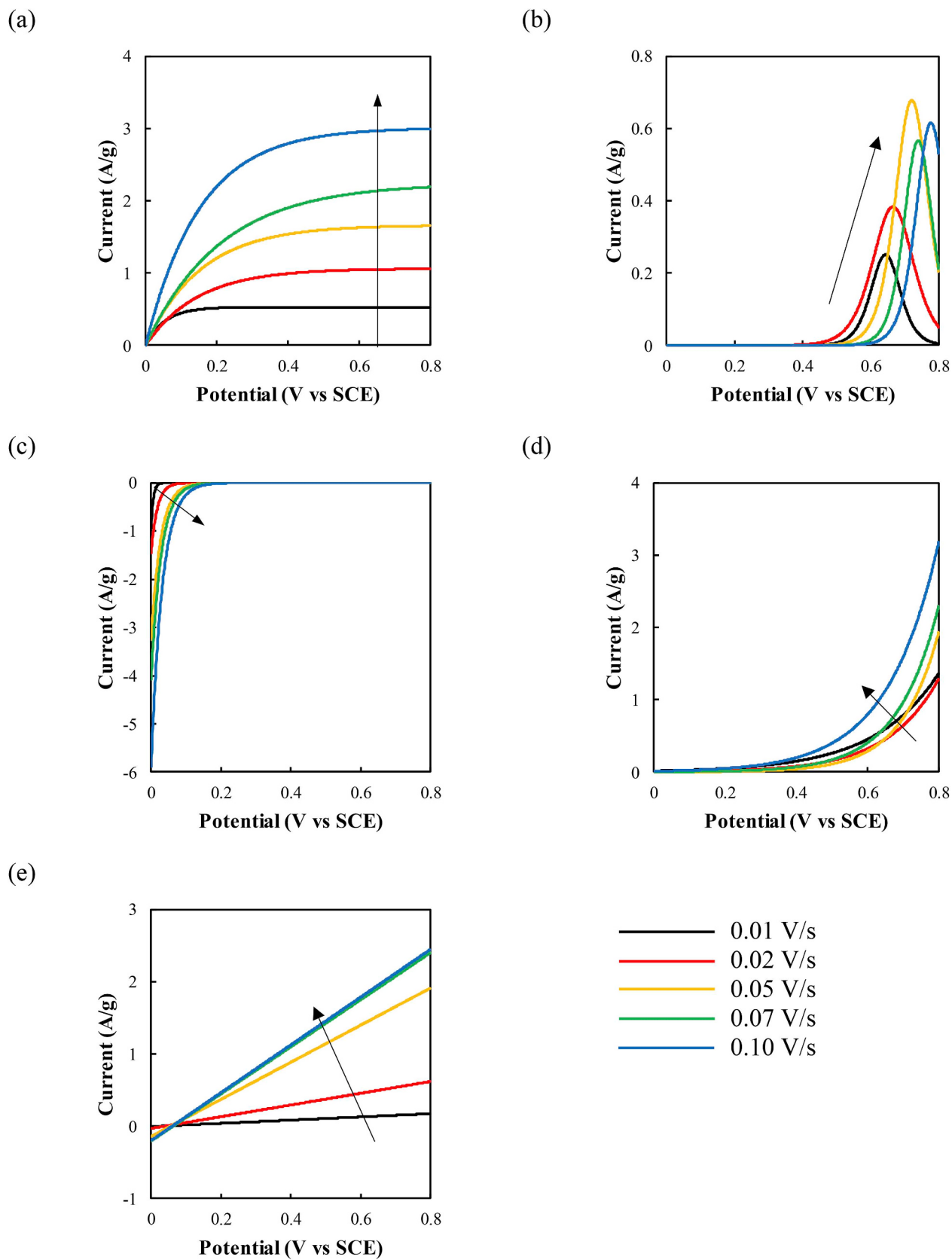


Fig. 5. Breakdown of the anodic voltammetric data into contributions from (a) a series RC component, (b) a cathodic Butler-Volmer (BV) term, (c) an anodic Butler-Volmer (BV) term, (d) a redox peak, and (e) an ohmic current.

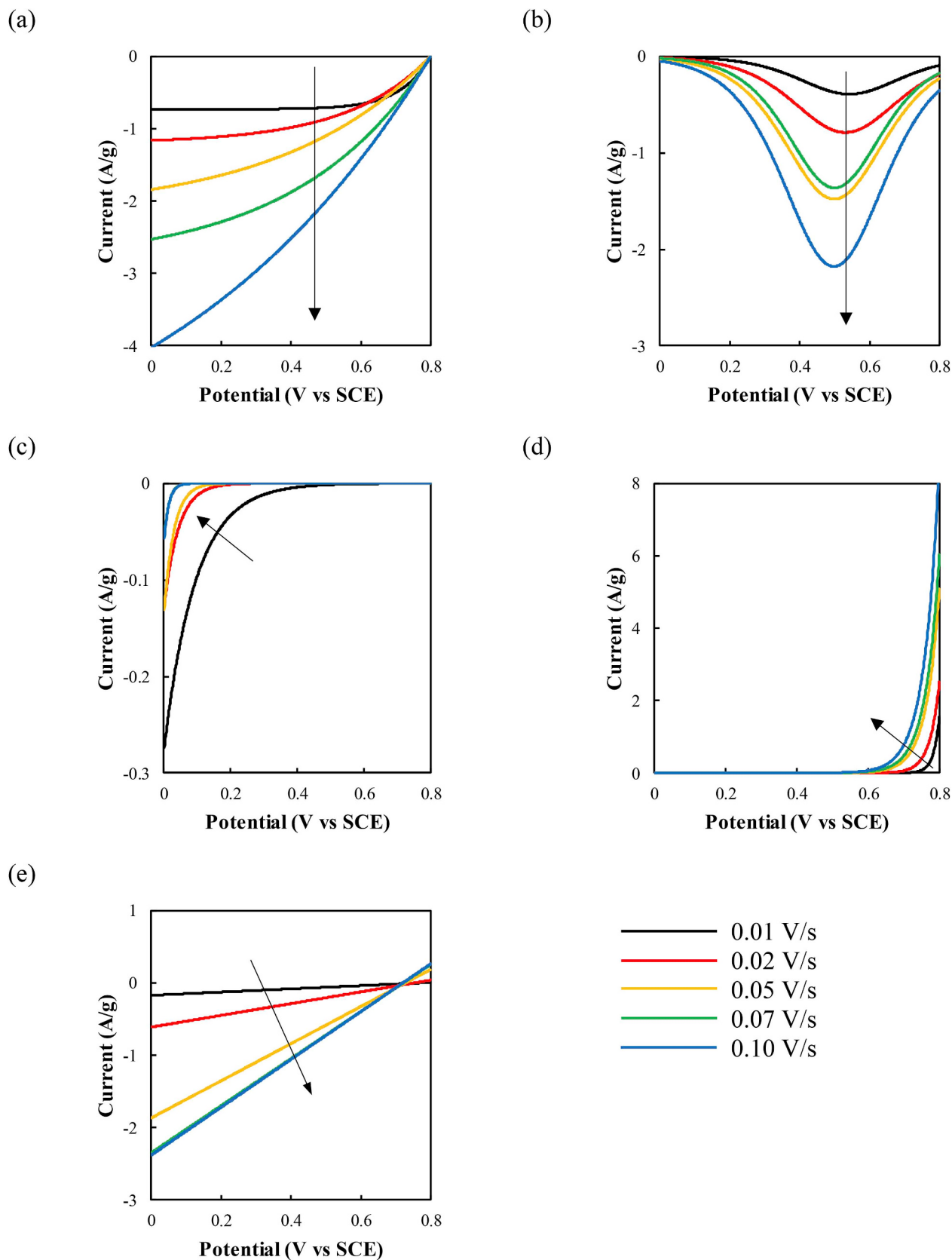


Fig. 6. Breakdown of the cathodic voltammetric data into contributions from (a) a series RC component, (b) a cathodic Butler-Volmer (BV) term, (c) an anodic Butler-Volmer (BV) term, (d) a redox peak, and (e) an ohmic current.

Table 1
RC circuit component.

Sweep Rate	Anodic					Cathodic				
	R	C	τ	C_{Expt}	X_C	R	C	τ	C_{Expt}	X_C
(V/s)	($\Omega \cdot \text{g}$)	(F/g)	(s)	(F/g)	(Eq. (8))	($\Omega \cdot \text{g}$)	(F/g)	(s)	(F/g)	(Eq. (8))
0.01	0.102	52.9	5.4	49.3	0.933	0.118	73.2	8.6	65.2	0.891
0.02	0.138	53.1	7.3	43.4	0.818	0.195	60.2	11.7	43.0	0.715
0.05	0.093	33.3	3.1	26.9	0.808	0.196	43.5	8.5	23.8	0.548
0.07	0.094	32.0	3.0	23.7	0.742	0.131	41.1	5.4	24.0	0.584
0.10	0.051	30.1	1.5	24.4	0.810	0.124	62.8	7.8	23.4	0.374
										0.024

Table 2
Peak.

Sweep Rate	Anodic				Cathodic			
	n	M	E°	C_R	n	M	E°	C_R
(V/s)		(mol)	(V vs SCE)	(C/g)		(mol)	(V vs SCE)	(C/g)
0.01	0.885	3.4×10^{-5}	0.644	3.6	0.266	5.9×10^{-4}	0.541	17.6
0.02	0.638	5.0×10^{-5}	0.666	3.7	0.258	6.3×10^{-4}	0.530	18.4
0.05	0.786	2.3×10^{-5}	0.721	2.0	0.270	4.3×10^{-4}	0.499	13.4
0.07	0.914	1.0×10^{-5}	0.740	1.0	0.288	2.5×10^{-4}	0.500	8.4
0.10	0.873	8.6×10^{-6}	0.777	0.6	0.266	3.3×10^{-4}	0.498	10.0

Table 3
Cathodic BV.

Sweep Rate	Anodic				Cathodic			
	i_o	α_c	E°	C_R	i_o	α_c	E°	C_R
(V/s)	(A/g)		(V vs SCE)	(F/g)	(A/g)		(V vs SCE)	(F/g)
0.01	0.291	4.185	0.007	0.73	0.225	0.272	0.020	3.23
0.02	0.605	1.468	0.015	1.59	0.096	0.603	0.013	0.34
0.05	0.620	0.956	0.045	2.18	0.094	0.859	0.011	0.10
0.07	0.695	0.898	0.050	2.08	0.035	1.790	0.008	0.01
0.10	0.796	0.813	0.063	2.33	0.035	1.783	0.008	0.01

Table 4
Anodic BV.

Sweep Rate	Anodic Sweep				Cathodic Sweep			
	i_o	α_a	E°	C_R	i_o	α_a	E°	C_R
(V/s)	(A/g)		(V vs SCE)	(C/g)	(A/g)		(V vs SCE)	(C/g)
0.01	0.249	0.142	0.492	30.50	0.003	1.550	0.698	3.19
0.02	0.194	0.179	0.528	11.54	0.006	0.947	0.637	4.25
0.05	0.244	0.244	0.583	5.07	0.003	0.689	0.521	4.74
0.07	0.197	0.223	0.517	4.72	0.002	0.652	0.487	4.23
0.10	0.213	0.178	0.410	5.72	0.002	0.620	0.455	4.47

Table 5
Ohmic.

Sweep Rate	Anodic Sweep				Cathodic Sweep			
	Slope	R_{ohm}	K	C_R	K	C_R		
(V/s)	($A^{-1} \cdot g$)	($\Omega \cdot g$)	(A/g)	(F/g)	(A/g)	(F/g)		
0.01	0.222	4.505	-0.003	8.56	-0.172	8.26		
0.02	0.810	1.235	-0.029	14.73	-0.611	14.29		
0.05	2.563	0.390	-0.140	17.70	-1.866	16.76		
0.07	3.252	0.308	-0.203	15.69	-2.347	14.90		
0.10	3.302	0.303	-0.196	11.25	-2.379	10.55		

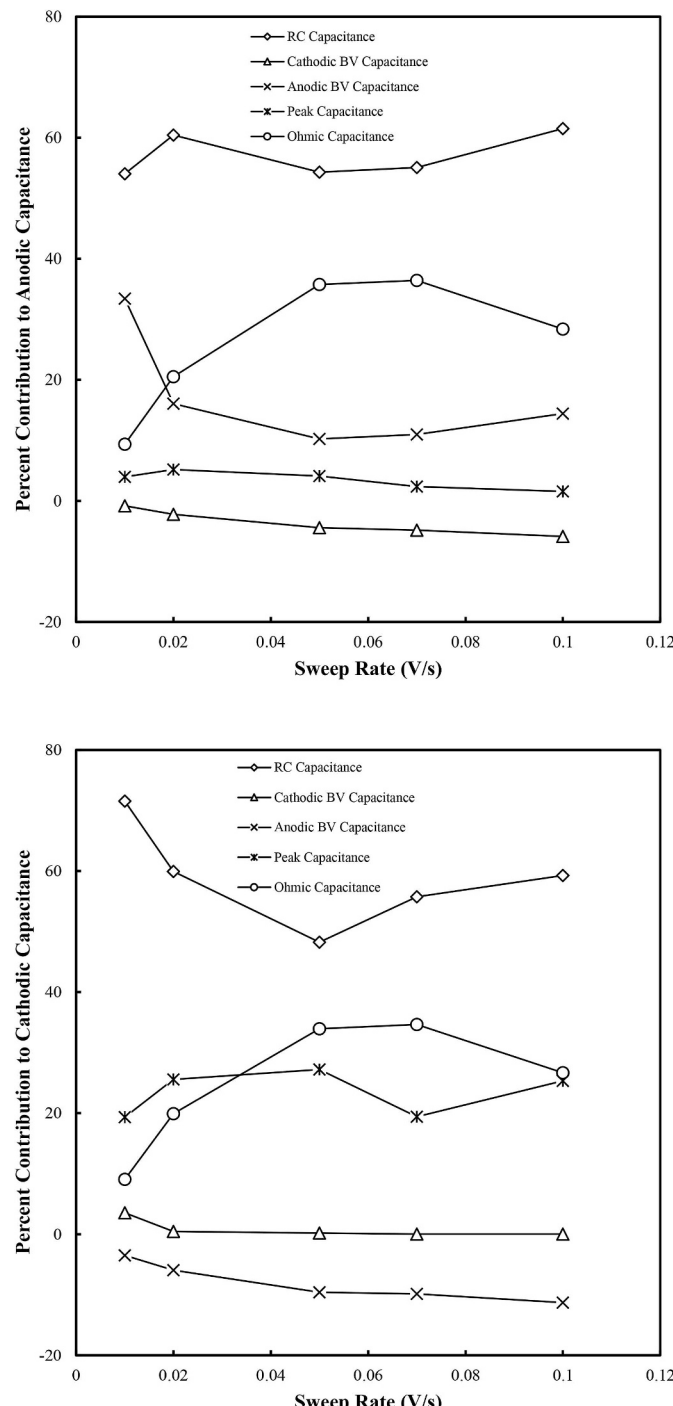


Fig. 7. Percent contributions made by the various components to the overall (a) anodic and (b) cathodic capacitance.

3.3.2. Redox processes in specific domains

The contributions to the total current by the redox peak fit to the voltammetric data is shown in Fig. 5(b) for the anodic sweep and Fig. 6(b) for the cathodic sweep. Specific parameters and the resultant capacitance for these peaks are shown in Table 2, while their contributions to the total capacitance are shown in Fig. 7.

Pseudo-capacitance within an electrochemical capacitor system is due to facile redox processes at or near the electrode-electrolyte interface. These processes can be delocalized across the entire electrode-electrolyte interface, such as was examined using the series RC

component, or localized and associated with specific redox processes that have a well-defined discrete potential. When these species undergo electrochemical oxidation or reduction the resultant current flows over a relatively narrow potential window. Manganese dioxide is an example of an electrode material that exhibits both delocalized and localized charge storage. The expression in Eq.(20) has been used to model the contribution of localized charge storage processes in the aqueous manganese dioxide electrode.

During the anodic half-cycle the current generated from this redox process increased with sweep rate up until 0.07 and 0.10 V/s, at which point the current became relatively constant. The increasing current here is consistent with conventional electrochemical kinetics, but the subsequent current plateau is likely due to the emergence of other electrochemical processes competing better for the available charge (see later). It is also apparent the potential of these redox processes is shifting to more anodic potentials (Table 2). This is consistent with the observed voltammetric behaviour in Fig. 1 where it is clear that the anodic peak is shifting to higher potentials. This peak shift is likely due to sluggish redox kinetics leading to a greater reaction overpotential at higher sweep rates. This is supported by the amount of species being oxidized (Table 2) which also decreases as the sweep rate increases. The value of n for this process is approximately constant at ~0.82 indicating that this process occurs over a rather narrow potential window. Furthermore, the capacitance from this process is quite limited, decreasing from 3.6 C/g to 0.6 C/g as the sweep rate is increased from 0.01 to 0.10 V/s (Table 2), which represents only ~3% to the overall anodic capacitance (Fig. 7).

The cathodic redox peaks extracted from the cathodic data show considerable differences compared to the corresponding anodic process. Firstly, the peak is quite broad covering a large potential window, as indicated by the small value for n (on average 0.27) in Table 2. The moles of material reduced in this process was also considerably larger than in the anodic process, at least an order of magnitude more, indicating that additional material was being reduced, which is likely the result of another underlying anodic process to be discussed shortly. There was also little shift in the potential of this process with increasing sweep rate (Table 2). The peak potential was 0.541 V versus SCE when the slowest sweep rate was used; however, this became constant at 0.500 V versus SCE when 0.05 V/s and faster sweep rates were used, perhaps highlighting the reduction of multiple different species. In general the capacitance from this process decreased with increasing sweep rate, ranging from 17.6 F/g with 0.01 V/s to 10.0 F/g with 0.10 V/s. This was much more substantial compared to the anodic process, equating to ~23% of the overall cathodic capacitance.

3.3.3. Cathodic Butler-Volmer processes

Towards the lower potential limit in the voltammetric data electrochemical processes have been modelled by a cathodic Butler-Volmer expression (Eq.(21)). It is important to note here that for the anodic half-cycle these processes detract from the electrode capacitance, while for the cathodic half-cycle they contribute positively. The contributions made by this component to the overall current are shown in Figs. 5(c) and 6(c) for the anodic and cathodic half-cycles, respectively, with specific parameters and capacitance data in Table 3, and their contributions to the total capacitance in Fig. 7.

During the initial stages of the anodic sweep a cathodic current was evident in the experimental voltammetric data due to residual cathodic charge storage processes. We have modelled this using a cathodic Butler-Volmer expression to provide insight firstly into the response of these cathodic processes, as well as to examine their contribution to the overall capacitance. Fig. 5(c) shows that the modelled cathodic current extracted from the experimental voltammetric data during the initial stages of the anodic sweep. As can be seen the current increases with increasing sweep rate which has the added effect of broadening the potential window over which these cathodic processes are evident. This is supported firstly by the increasing exchange current density (i_0) for

the process, as well as by the increasing equilibrium potential (E°) as the sweep rate increases (Table 3). The cathodic transfer coefficient (α_c) is an indicator of the rate of change of current with changes in potential, as well as possibly the mechanisms of charge storage, and its decreasing value with increasing sweep rate is indicative of limited electrochemical kinetics. The capacitance of this process was very small, ranging from 0.73 C/g with 0.01 V/s up to 2.33 C/g with 0.10 V/s. These processes detract from the overall anodic capacitance, increasing at higher sweep rates due to the limited kinetics of these processes. This represents ~3% reduction in the anodic capacitance.

For the cathodic half-cycle the inclusion of a cathodic Butler-Volmer expression contributes positively to the overall current and cathodic capacitance; however, their contributions are very modest. As shown in Fig. 6(c), this is the one example here of where the current decreased with increasing sweep rate. This is an example of where kinetic limitations or increasing overpotential are hampering the redox process by shifting it to lower potentials outside the potential window under study. This is supported by the fitting parameters in Table 3, in particular a decreasing exchange current density and a cathodic-shifting equilibrium potential. The capacitance contributed by this process is also modest, being at most 3.23 F/g at the slowest sweep rate, and dropping significantly at higher rates. On average, this equates to ~0.9% of the total cathodic capacitance. The origins of this cathodic process are likely associated with the continuing reduction of manganese dioxide, rather than alternate cathodic processes like hydrogen evolution because the potential for this process is too low to fall within the potential window used here. Given that it is towards the lower potential limit and in a neutral aqueous electrolyte it may be associated with the reduction of manganese dioxide to a Mn(II) containing species.

3.3.4. Anodic Butler-Volmer processes

Towards the upper potential limit in the cyclic voltammetry experiments an anodic Butler-Volmer expression was used to model the electrochemical processes occurring. During the anodic half-cycle these processes contribute positively to the capacitance; however, during the cathodic half cycle they contribute negatively to performance. The contributions made by the anodic Butler-Volmer expression to the total current are shown in Figs. 5(d) and 6(d) for the anodic and cathodic half-cycles, respectively, which Fig. 7(a) and (b) show the contributions of this process to the total anodic and cathodic capacitance, respectively. Individual parameters are also shown in Table 4.

The open circuit potential for the electrolytic manganese dioxide electrode in the aqueous K_2SO_4 electrolyte used here is ~0.4 V versus SCE, as measured as the rest potential of the electrode system before any electrochemistry is carried out. At this point the starting material is notionally manganese dioxide (MnO_2) and so in principle sweeping the potential to higher values leads to either the further oxidation of the manganese dioxide or possibly the evolution of oxygen from the electrode surface. The oxidation of manganese dioxide to higher valent manganese species is unlikely because in neutral media the potential required is too high [60]. What is more likely however, is the oxidation of the electrolyte to form molecular oxygen. Given the standard redox potential for manganese dioxide formation from Mn^{2+} and oxygen evolution from water are comparable [60,61], this is a distinct possibility. This would of course be a catastrophic event in a sealed cell, and so further investigation is required here. Another possible, perhaps even probable, cause of this process is the slow kinetics of the redox processes associated with the manganese dioxide electrode. With extended cycling the relatively slow redox processes in the manganese dioxide electrode, particularly diffusion-based processes in a neutral medium, are likely to accrue charge which can only be released at the extremes of potential. The higher anodic capacitance dissipated at the slowest sweep rate is indicative of a better recovery of charge, whereas at the faster sweep rates only a small fraction of the capacitance is recovered. During the anodic sweep the contributions this process made to the overall capacitance exhibited a minimum at intermediate sweep rates of

~10%, while at slow sweep rates it contributed ~35% and at fast sweep rates it contributed ~18%. During the cathodic sweep a relatively constant capacitance was recovered before the overall process became cathodic. These anodic processes detracted from the total cathodic capacitance by ~4% at the slowest sweep rate, up to ~12% at the fastest sweep rate.

3.3.5. Electrode resistance

The final process contributing to electrode behaviour was due to an ohmic resistance process. Here it is important to differentiate between a series resistance that is associated with a charge storage process, such as with double layer formation (Eq.(6)), and a resistance that is associated with the overall electrode. The first is specific to a process, while the latter is associated with overall electrode behaviour. The origin of this process is to do with the resistance of the electrode materials as well as the construction of the electrode, and in general is what gives rise to the gradual positive slope seen in the voltammetric data. Figs. 5(e) and 6(e) show the current flow due to these resistive processes during the anodic and cathodic half-cycles, respectively, while Fig. 7(a) and (b) show the fractional contribution these processes make to the overall anodic and cathodic capacitance, respectively. Table 5 contains specific fitting parameters for these processes. It is also important to recall here that during the fitting the slope of this process was kept constant for both the anodic and cathodic half-cycles, and that the fitted line passed through the point when zero current was recorded for the respective half-cycles. The reasons for these restrictions were outlined previously.

The total current for these processes in Figs. 5(e) and 6(e) show that as the sweep rate is increased the current reaches a plateau for the fastest sweep rates. The main implication of this is that it seems as though there is a self-imposed maximum current that can be reached for this process, beyond which it can no longer contribute to the overall current. This plateau in current is reflected in the fractional contributions these processes make to the overall anodic and cathodic capacitance (Fig. 7), which reaches a maximum at sweep rates between 0.05 and 0.07 V/s. The contributions made by these processes are also substantial, reaching a maximum of ~35%. Furthermore, the inverse of the slope represents the electrode resistivity, as per Eq.(22), which in this instance reaches a plateau at ~0.3 Ω g, which is a value typical of these electrode systems [45].

4. Summary and conclusions

Cyclic voltammetry is one of the most common methods for examining electrochemical capacitor materials and systems. It can be used to provide performance data and mechanistic information about the system under study. To improve the value of this technique we have developed an approach to deconvolute the various contributions to the overall voltametric response. This approach has been demonstrated through application to an aqueous manganese dioxide electrode. These contributions are based on:

- A series RC circuit representing electrical double layer formation;
- A Nernst equation derived expression representing redox processes in a localized energy domain;
- The Butler-Volmer equation to describe redox processes at the extremes of potential typically associated with electrode instability; and
- The ohmic resistance of the electrode.

Overall, the comparison between the experimental and modelled data was very good, with the resultant parameters being consistent with existing knowledge about the aqueous manganese dioxide electrode, thus providing a more detailed quantitative assessment of electrode voltammetric data.

Acknowledgements

The University of Newcastle is acknowledged for the provision of PhD scholarship (MF). The University of Nantes is also acknowledged for the provision of funding to support Visiting Professors (SWD).

References

- [1] A.M. Omer, Energy, environment and sustainable development, *Renew. Sustain. Energy Rev.* 12 (9) (2008) 2265–2300.
- [2] M. Dresselhaus, I. Thomas, Alternative energy technologies, *Nature* 414 (6861) (2001) 332.
- [3] K. Kaygusuz, Energy for sustainable development: a case of developing countries, *Renew. Sustain. Energy Rev.* 16 (2) (2012) 1116–1126.
- [4] B. Lin, B. Xu, How to promote the growth of new energy industry at different stages? *Energy Pol.* 118 (2018) 390–403.
- [5] R.K. Singh, A. Sarkar, J.P. Chakraborty, Influence of Alternate Fuels on the Performance and Emission from Internal Combustion Engines and Soot Particle Collection Using Thermophoretic Sampler: a Comprehensive Review, *Waste and Biomass Valorization*, 2018, pp. 1–23.
- [6] P.J. Hall, E.J. Bain, Energy-storage technologies and electricity generation, *Energy Pol.* 36 (12) (2008) 4352–4355.
- [7] P. Simon, Y. Gogotsi, Materials for electrochemical capacitors, *Nat. Mater.* 7 (11) (2008) 845–854.
- [8] B. Dunn, H. Kamath, J.-M. Tarascon, Electrical energy storage for the grid: a battery of choices, *Science* 334 (6058) (2011) 928–935.
- [9] P.J. Hall, et al., Energy storage in electrochemical capacitors: designing functional materials to improve performance, *Energy Environ. Sci.* 3 (9) (2010) 1238–1251.
- [10] M.F. Dupont, S.W. Donne, Charge storage mechanisms in electrochemical capacitors: effects of electrode properties on performance, *J. Power Sources* 326 (2016) 613–623.
- [11] M. Endo, et al., Capacitance and pore-size distribution in aqueous and nonaqueous electrolytes using various activated carbon electrodes, *J. Electrochem. Soc.* 148 (8) (2001) A910–A914.
- [12] M.F. Dupont, S.W. Donne, A step potential electrochemical spectroscopy analysis of electrochemical capacitor electrode performance, *Electrochim. Acta* 167 (2015) 268–277.
- [13] M.F. Dupont, S.W. Donne, Separating faradaic and non-faradaic charge storage contributions in activated carbon electrochemical capacitors using electrochemical methods: I. Step potential electrochemical spectroscopy, *J. Electrochem. Soc.* 162 (7) (2015) A1246–A1254.
- [14] G. Xu, et al., Binder-free activated carbon/carbon nanotube paper electrodes for use in supercapacitors, *Nano Research* 4 (9) (2011) 870–881.
- [15] M. Zhi, et al., Effects of pore structure on performance of an activated-carbon supercapacitor electrode recycled from scrap waste tires, *ACS Sustain. Chem. Eng.* 2 (7) (2014) 1592–1598.
- [16] X. He, et al., Preparation of microporous activated carbon and its electrochemical performance for electric double layer capacitor, *J. Phys. Chem. Solid.* 70 (3) (2009) 738–744.
- [17] M. Inagaki, H. Konno, O. Tanaike, Carbon materials for electrochemical capacitors, *J. Power Sources* 195 (24) (2010) 7880–7903.
- [18] E.T. Mombeshora, V.O. Nyamori, A review on the use of carbon nanostructured materials in electrochemical capacitors, *Int. J. Energy Res.* 39 (15) (2015) 1955–1980.
- [19] V. Khomenko, E. Raymundo-Piñero, F. Béguin, High-energy density graphite/AC capacitor in organic electrolyte, *J. Power Sources* 177 (2) (2008) 643–651.
- [20] L.L. Zhang, X. Zhao, Carbon-based materials as supercapacitor electrodes, *Chem. Soc. Rev.* 38 (9) (2009) 2520–2531.
- [21] E. Frackowiak, F. Béguin, Carbon materials for the electrochemical storage of energy in capacitors, *Carbon* 39 (6) (2001) 937–950.
- [22] H. Zhang, G. Cao, Y. Yang, Carbon nanotube arrays and their composites for electrochemical capacitors and lithium-ion batteries, *Energy Environ. Sci.* 2 (9) (2009) 932–943.
- [23] V. Barranco, et al., Amorphous carbon nanofibers and their activated carbon nanofibers as supercapacitor electrodes, *J. Phys. Chem. C* 114 (22) (2010) 10302–10307.
- [24] K. Okajima, et al., High rate performance of highly dispersed C60 on activated carbon capacitor, *Electrochim. Acta* 51 (5) (2005) 972–977.
- [25] D. Pech, et al., Ultrahigh-power micrometre-sized supercapacitors based on onion-like carbon, *Nat. Nanotechnol.* 5 (9) (2010) 651.
- [26] Y. Wang, Y. Song, Y. Xia, Electrochemical capacitors: mechanism, materials, systems, characterization and applications, *Chem. Soc. Rev.* 45 (21) (2016) 5925–5950.
- [27] G. Wang, L. Zhang, J. Zhang, A review of electrode materials for electrochemical supercapacitors, *Chem. Soc. Rev.* 41 (2) (2012) 797–828.
- [28] C.-C. Hu, W.-C. Chen, K.-H. Chang, How to achieve maximum utilization of hydrous ruthenium oxide for supercapacitors, *J. Electrochem. Soc.* 151 (2) (2004) A281–A290.
- [29] A. Cross, et al., Enhanced manganese dioxide supercapacitor electrodes produced by electrodeposition, *J. Power Sources* 196 (18) (2011) 7847–7853.
- [30] Q. Meng, et al., Research progress on conducting polymer based supercapacitor electrode materials, *Nano Energy* 36 (2017) 268–285.
- [31] B.E. Conway, *Electrochemical Supercapacitors. Scientific Fundamentals and Technological Applications*, Kluwer Academic/Plenum Publishers, New York, 1999.
- [32] X. Yang, et al., Functionalized porous carbon with appropriate pore size distribution and open hole texture prepared by H₂O₂ and EDTA-2Na treatment of loofa sponge and its excellent performance for supercapacitors, *RSC Adv.* 6 (6) (2016) 4365–4376.
- [33] D. Qu, H. Shi, Studies of activated carbons used in double-layer capacitors, *J. Power Sources* 74 (1) (1998) 99–107.
- [34] M. Demir, S.K. Sarawat, R.B. Gupta, Hierarchical nitrogen-doped porous carbon derived from lecithin for high-performance supercapacitors, *RSC Adv.* 7 (67) (2017) 42430–42442.
- [35] S. Sarangapani, B. Tilak, C.P. Chen, Materials for electrochemical capacitors theoretical and experimental constraints, *J. Electrochem. Soc.* 143 (11) (1996) 3791–3799.
- [36] M.F. Dupont, S.W. Donne, Separating the faradaic and non-faradaic contributions to the total capacitance for different manganese dioxide phases, *J. Electrochem. Soc.* 162 (5) (2015) A5096–A5105.
- [37] J.W. Long, et al., Voltammetric characterization of ruthenium oxide-based aerogels and other RuO₂ solids: the nature of capacitance in nanostructured materials, *Langmuir* 15 (3) (1999) 780–785.
- [38] H.Y. Lee, S. Kim, H.Y. Lee, Expansion of active site area and improvement of kinetic reversibility in electrochemical pseudocapacitor electrode, *Electrochim. Solid State Lett.* 4 (3) (2001) A19–A22.
- [39] B. Sethuraman, K.K. Purushothaman, G. Muralidharan, Synthesis of mesh-like Fe 2 O 3/C nanocomposite via greener route for high performance supercapacitors, *RSC Adv.* 4 (9) (2014) 4631–4637.
- [40] D. Ahn, et al., Polyaniiline nanocoating on the surface of layered Li [Li_{0.2}CoO₂·1Mn_{0.7}]O₂ nanodisks and enhanced cyclability as a cathode electrode for rechargeable lithium-ion battery, *J. Phys. Chem. C* 114 (8) (2010) 3675–3680.
- [41] H.D. Abruna, Y. Kiya, J.C. Henderson, Batteries and electrochemical capacitors, *Phys. Today* 61 (12) (2008) 43–47.
- [42] W. Shimizu, et al., Development of a 4.2 V aqueous hybrid electrochemical capacitor based on MnO₂ positive and protected Li negative electrodes, *J. Power Sources* 241 (2013) 572–577.
- [43] K. Kierzek, et al., Electrochemical capacitors based on highly porous carbons prepared by KOH activation, *Electrochim. Acta* 49 (4) (2004) 515–523.
- [44] P. Taberna, P. Simon, J.-F. Fauvarque, Electrochemical characteristics and impedance spectroscopy studies of carbon-carbon supercapacitors, *J. Electrochem. Soc.* 150 (3) (2003) A292–A300.
- [45] M.F. Dupont, A.F. Hollenkamp, S.W. Donne, Large amplitude electrochemical impedance spectroscopy for characterizing the performance of electrochemical capacitors, *J. Electrochem. Soc.* 161 (4) (2014) A648–A656.
- [46] M. Forghani, S.W. Donne, Method comparison for deconvoluting capacitive and pseudo-capacitive contributions to electrochemical capacitor electrode behavior, *J. Electrochem. Soc.* 165 (3) (2018) A664–A673.
- [47] M. Forghani, S.W. Donne, Duty cycle effects on the step potential electrochemical spectroscopy (SPECs) analysis of the aqueous manganese dioxide electrode, *J. Electrochim. Soc.* 165 (3) (2018) A593–A602.
- [48] M.F. Dupont, et al., Effect of electrolyte cation on the charge storage mechanism of manganese dioxide for electrochemical capacitors, *Electrochim. Acta* 271 (2018) 337–350.
- [49] M.F. Dupont, S.W. Donne, Electrolytic manganese dioxide structural and morphological effects on capacitive performance, *Electrochim. Acta* 191 (2016) 479–490.
- [50] M.F. Dupont, S.W. Donne, Faradaic and non-faradaic contributions to the power and energy characteristics of electrolytic manganese dioxide for electrochemical capacitors, *J. Electrochim. Soc.* 163 (6) (2016) A888–A897.
- [51] S.-B. Yoon, et al., Study on the electrochemical kinetics of manganese dioxide/multiwall carbon nanotube composite by voltammetric charge analysis, *J. Electrochim. Soc.* 161 (1) (2014) A137–A141.
- [52] A.J. Bard, L.R. Faulkner, *Electrochemical Methods: Fundamentals and Applications*, John Wiley and Sons, 1980.
- [53] G.J. Browning, S.W. Donne, Electrochemical kinetic behaviour of the aqueous manganese dioxide electrode, *J. Appl. Electrochim.* 35 (2005) 437–443.
- [54] V.V. Sizov, et al., Redox transformations in electroactive polymer films derived from complexes of nickel with Salen-type ligands: computational, EQCM, and spectroelectrochemical study, *J. Solid State Electrochim.* 19 (2) (2015) 453–468.
- [55] Kendall, K. and M. Kendall, *High-temperature Solid Oxide Fuel Cells for the 21st Century - Fundamentals, Design and Applications*. Elsevier.
- [56] Y. He, et al., Capacitive mechanism of oxygen functional groups on carbon surface in supercapacitors, *Electrochim. Acta* 282 (2018) 618–625.
- [57] H.-B. Gu, et al., Electrochemical properties of carbon composite electrode with polymer electrolyte for electric double-layer capacitor, *Electrochim. Acta* 45 (8) (2000) 1533–1536.
- [58] J.H. Jang, et al., Electrochemical capacitor performance of hydrous ruthenium oxide/mesoporous carbon composite electrodes, *J. Power Sources* 123 (1) (2003) 79–85.
- [59] S.H. Aboutalebi, et al., Comparison of GO, GO/MWCNTs composite and MWCNTs as potential electrode materials for supercapacitors, *Energy Environ. Sci.* 4 (5) (2011) 1855–1865.
- [60] F.A. Armstrong, Why did Nature choose manganese to make oxygen? *Philos. Trans. R. Soc. Lond. B Biol. Sci.* 363 (1494) (2008) 1263–1270.
- [61] A. Shein, E. Zubova, Electrochemical behavior of manganese silicides in sulfuric acid solution, *Protect. Met.* 41 (3) (2005) 234–242.